# Boundary mixing by density overturns in an internal tidal beam

B. Gayen[1] and S. Sarkar[1]

[1] A numerical study based on large eddy simulation (LES) is performed to investigate near-bottom mixing processes in an internal wave beam over a critical slope. Transition to turbulence from an initial laminar state is followed by mixing events that occur at specific phases. Maximum turbulent kinetic energy and dissipation rate are found just after the zero velocity point when flow reverses from downslope to upslope motion. At this phase, convective instability leads to density overturns that originate in the upper flank of the beam and span the beam width of 60 m. Turbulence originating at the bottom and with smaller vertical extent is also present during the phases of peak upslope and downslope flow when the boundary layer shear is large. The present numerical simulations identify and characterize a process, internal wave beam at a critical slope during generation or after propagation from a nearby generation site, that may lead to the high turbulence levels, modulated at the tidal frequency, that is observed near the bottom in oceanic sites with near-critical topography. **Citation:** Gayen, B., and S. Sarkar (2011), Boundary mixing by density overturns in an internal tidal beam, *Geophys. Res. Lett.*, *38*, L14608, doi:10.1029/2011GL048135.

## 1. Introduction

[2] Localized regions of high boundary turbulence play an important role in setting average diapycnal mixing rates necessary to maintain the vertical stratification observed in the mid-ocean. Bottom boundary turbulence is enhanced at rough topography including sea-mounts [*Lueck and Mudge*, 1997; *Kunze and Toole*, 1997], submarine ridges [*Rudnick et al.*, 2003; *Aucan et al.*, 2006; *Levine and Boyd*, 2006; *Klymak et al.*, 2006], continental slopes [*Thorpe et al.*, 1990; *Moum et al.*, 2002; *Nash et al.*, 2007] and deep rough topography [*Polzin et al.*, 1997; *St. Laurent et al.*, 2001]. Measurements of currents, vertical displacements and turbulent dissipation rate at these sites often show a dominant modulation by internal tides that are generated by surface tides that oscillate over topographic features. Therefore, there is much current interest in understanding bottom turbulence processes associated with internal waves at sloping topography.

[3] Observations indicate that bottom turbulence, with order 100 m density overturns, is present at or near regions with critical slope where the slope angle, $\beta$, is approximately equal to the inclination, $\theta$, of internal wave phase lines with the horizontal. *Moum et al.* [2002], using a towed body package that included turbulence sensors, found a large 5 km lateral extent of turbulent flow within a few hundred meters

off a sloping region that is critical to the M2 internal tide. The dissipation profile averaged over the survey exhibited a value of $10^{-9}$ W/kg at 500 mab which is 10 times the open ocean value while the values closer to the bottom were about 100 times lager than the open ocean value. *Aucan et al.* [2006] examined tidal variations within 200 m of a deep (2425 m) flank of Kaena Ridge as part of the Hawaii Ocean Mixing Experiment (HOME). A series of temperature sensors detected tidally driven overturns with vertical scales of order 100 m and peak near-bottom dissipation of $2 \times 10^{-6}$ W/kg inferred by Thorpe-scale analysis. The time-averaged dissipation was $1.2 \times 10^{-8}$ W/kg, about 10–100 times the value in the ocean interior at similar depths and 50 km from the ridge. Furthermore, *Aucan et al.* [2006] found that enhanced dissipation occurred at specific phases of the internal tide. *Nash et al.* [2007] reported two deep ocean hotspots of turbulent mixing, both at near-critical regions of the Oregon continental slope, where they estimated time-averaged turbulent energy dissipation rates of $10^{-7}$ Wkg$^{-1}$ and eddy diffusivities of $K_\rho = 10^{-2}$ m$^2$/s.

[4] During the generation of internal tides at critical slopes, high vertical number modes are formed that combine to give internal tidal beams. Laboratory [*Lim et al.*, 2010] and numerical [*Gayen and Sarkar*, 2010, 2011] experiments have shown evidence of turbulence in tidal beams over slope topography with length of the order $\mathcal{O}(1$–$30)$ m. However, the beam was at laboratory scale (width smaller than 0.2 m) and did not allow the large separation in scales between the viscous boundary layer and the oscillating core of the beam that occurs in the ocean. The objective of the present work is to numerically model a near-bottom beam with a larger, more realistic width and characterize its turbulence characteristics. We will also show that the phase dependence of turbulence in the numerical model agrees with that observed by *Aucan et al.* [2006] off Kaena Ridge and try to explain the underlying mechanism.

## 2. Problem Set Up

[5] The boundary-conforming grid, curvilinear coordinates, and streamwise inhomogeneity in our earlier studies [*Gayen and Sarkar*, 2010, 2011] enabled accurate simulation of internal wave beam formation at a slope in response to the imposed barotropic forcing and subsequent formation of turbulence. In the present work, we assume that there is a beam with a given width, $l_b$, and peak near-bottom velocity, $U_b$, on a slope and simulate phase-dependent turbulence in a small patch of the beam. It would be impractical to perform a turbulence-resolving simulation in a streamwise non-periodic domain with the large slope length of several hundred meters that is required for beam generation with $l_b = 60$ m.

[6] Large-eddy simulation (LES) is used to obtain the filtered velocity and temperature fields by numerical solu-

[1] Mechanical and Aerospace Engineering Department, University of California, San Diego, La Jolla, California, USA.
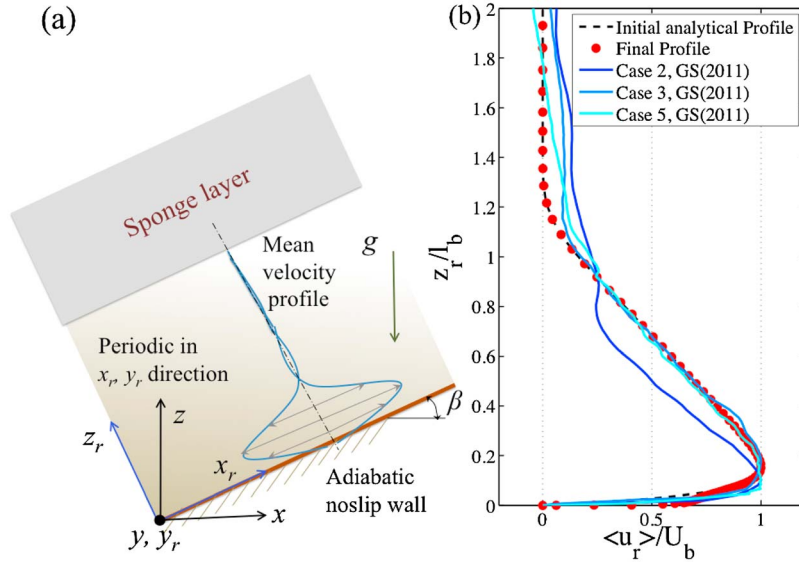
**Figure 1.** (a) Schematic of the problem. Background color shade indicates the stable density stratification. (b) Profiles of cross slope velocity, normalized with peak beam velocity $U_b$, as a function of normalized height ($z_r/l_b$) above bottom are shown for peak upslope flow. Velocity profiles for case 2, 3 and 5 with different slope lengths of 3.5 m, 7.2 m, and 25 m, respectively, are taken from *Gayen and Sarkar* [2011] to show approximately self-similar behavior in the previous work, and a fit (also chosen to help initialize the present simulation) to the self-similar shape function, denoted by $u_{r,f}(z)$, is shown by a black dashed line.

tion of the Navier-Stokes equations under the Boussinesq approximation, written in rotated coordinates $[x_r, y_r, z_r]$ in dimensional form as:

$$\nabla_r \cdot \mathbf{u}_r = 0$$

$$\frac{D\mathbf{u}_r}{D_r t} = -\frac{1}{\rho_0}\nabla_r p^* + \nu\nabla_r^2 \mathbf{u}_r - \frac{g\rho^*}{\rho_0}[\sin\beta\mathbf{i} + \cos\beta\mathbf{k}] - \boldsymbol{\nabla}\cdot\boldsymbol{\tau}$$

$$\frac{D\rho^*}{D_r t} = \kappa\nabla_r^2\rho^* - (u_r\sin\beta + w_r\cos\beta)\frac{d\rho^b}{dz} - \boldsymbol{\nabla}\cdot\boldsymbol{\lambda} \quad (1)$$

Here, $p^*$ and $\rho^*$ denote *deviation* from the background pressure and density, respectively. The quantity $\tau$ that denotes the subgrid scale stress tensor and $\lambda$ that is the subgrid density flux are modeled as described by *Gayen et al.* [2010]. Briefly, $\tau$ is represented with a dynamic eddy viscosity model, and $\lambda$ with a dynamic eddy diffusivity model. Each subgrid model has a single Smagorinsky coefficient that is evaluated through a dynamic procedure that involves the introduction of an additional test filter. The coefficient is averaged over the homogeneous directions (slope-parallel plane). The NS equations are numerically solved to obtain the velocity in rotated coordinates $[u_r, v_r, w_r]$ and the deviations from background density and pressure using a mixed spectral/finite difference algorithm on a staggered grid. Spanwise and across slope derivatives are treated with a pseudo-spectral method, and the wall normal spatial derivatives are computed with second-order finite differences. A third-order Runge-Kutta-Wray method is used for time-stepping, and viscous terms are treated implicitly with the Crank-Nicolson method. The test domain, excluding the sponge region, consists of a rectangular box of 30 m length, 160 m height and 10 m width whose bottom boundary is coincident with the slope topography as shown in Figure 1a. The grid size in the test domain is $128 \times 620 \times 64$ in the $x_r, z_r$

and $y_r$ directions, respectively, with stretching in $z_r$ direction. The grid spacing ($\Delta x_r = 0.234$ m, $\Delta y_r = 0.157$ m, $\Delta z_{r,\mathrm{min}} = 0.0037$ m, $\Delta z_{r,\mathrm{max}} = 3.5$ m) is sufficient for LES as is confirmed by examining the spanwise and the streamwise spectra as shown in Figure 2. Periodicity is imposed in the spanwise, $y_r$, and streamwise, $x_r$, direction. Zero velocity and a zero value for wall-normal total density flux i.e. $d\rho/dz_r = 0$ are imposed at the bottom. The sponge region, with damping to the background state, contains 15 points, extends from 160 m to 200 m, and has a maximum $\Delta z_r = 5.59$ m.

[7] *Gayen and Sarkar* [2011] found that the beam width, $l_b$, and velocity amplitude, $U_b$, increased with increasing slope length, following a power-law dependence. The beam in the present simulation is initialized by taking advantage of the approximately self-similar velocity structure, when normalized with $l_b$ and $U_b$, that was previously found. At $t = 0$, there are neither velocity nor density fluctuations. In the work by *Gayen and Sarkar* [2010], an oscillating baro-
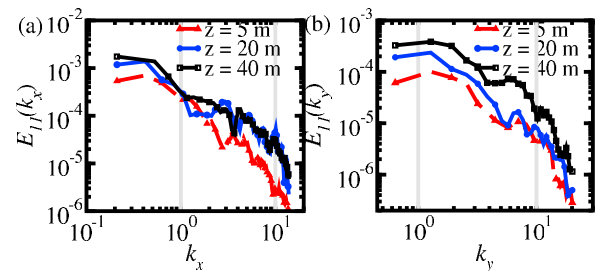


**Figure 2.** (a) Horizontally averaged $k_x$ spectra of the streamwise velocity fluctuation, $u'_r = u_r - \langle u_r \rangle$ at three heights from the bottom slope during flow reversal from downslope to upslope at $t = 16$ *hrs*. (b) Same as Figure 2a but for $k_y$ spectra.
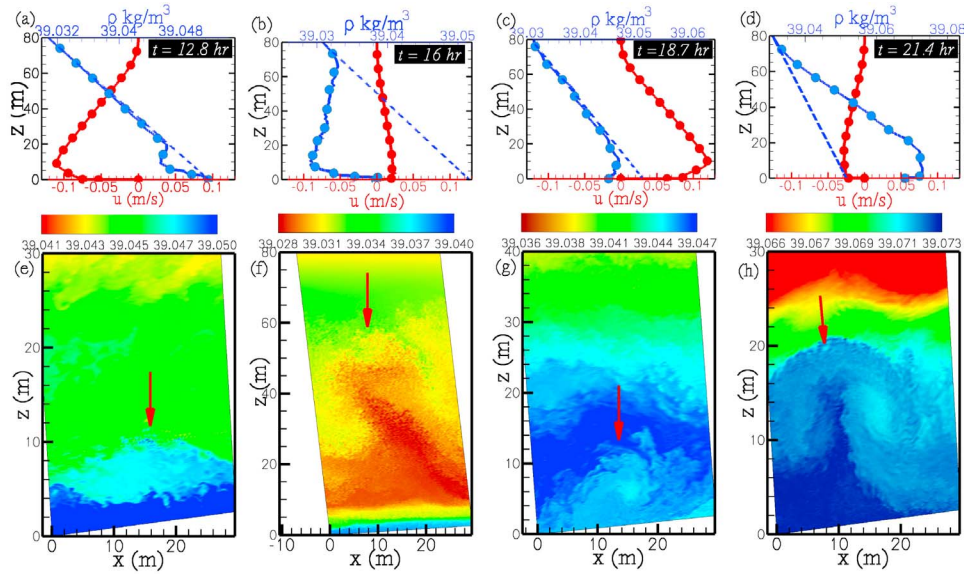
**Figure 3.** (e–h) Vertical $x$-$z$ slices of the density field (after subtracting 1000 kg m$^{-3}$) at 4 different times (phases) in a tidal cycle. (a–d) Spanwise-averaged streamwise velocities, $u$ ($z$, $t$) m/s and density profiles, $\rho(z, t, x = 0)$ at corresponding phases. Background linear density (dashed blue line) profile is also shown. Note that $u$, $x$ are horizontal while $z$ is vertical. Figures 3a and 3e correspond to maximum downward boundary flow, Figures 3b and 3f correspond to flow reversal from down to up, Figures 3c and 3g correspond to peak up-slope velocity and, finally, Figures 3d and 3h correspond to flow reversal from up to down. The four different times are indicated by the four red color circles in Figure 4a that follows. Here, arrows indicate the flow structures.

tropic tide with constant amplitude was prescribed on a near-critical slope, and the barotropic-to-baroclinic energy conversion compensated for the losses due to turbulent dissipation leading to a boundary jet with constant amplitude, $U_b$. In the current simulation, the amplitude, $U_b$, is maintained by adding a relaxation term, $-\sigma_f(z)[u_r(\mathbf{x}, t) - u_{r,f}(z)\cos(\Omega\, t)]$, to the right-hand side of the $x_r$ -momentum equation, with the target shape function, $u_{r,f}(z)$, plotted in Figure 1b. The shape of $\sigma_f(z)$ is such that the forcing is limited to the beam core, $z_r = 20$ m − 60 m, allowing the bottom boundary layer to develop independently. The imposed forcing is not shear unstable since the minimum gradient Richardson number, $Ri_g$, based on background velocity and stratification exceeds 0.5, larger than the critical value of $Ri_g = 0.25$. Owing to periodicity in the $x_r$ direction, mixed fluid recirculates in the computational domain so that turbulence at the flanks of the beam (caused by density overturns as will be shown) decreases after three tidal cycles. A simple way to overcome this limitation is to force $\rho$ towards the linear background during a short period (0.5 hour) when the downslope boundary flow is maximum by adding the function $-\sigma_f[\rho^*(\mathbf{x}, t)]$ to the evolution equation for $\rho^*$.

[8] In the present simulation, $N_\infty = 1.6 \times 10^{-3}$ rad s$^{-1}$ and $\Omega = 1.4076 \times 10^{-4}$ rad s$^{-1}$, which gives the wave angle $\theta = \sin^{-1}(\Omega/N_\infty) \approx 5°$. Slope angle $\beta = 5°$ sets the criticality parameter, $\epsilon = \tan\beta/\tan\theta \approx 1$. The kinematic viscosity, $\nu = 10^{-6}$ m$^2$/s, is that of water. The Prandtl number is chosen to be $Pr = 7$. The beam velocity amplitude is chosen to be $U_b = 0.125$ m/s and the beam width is $l_b = 60$ m. Cycle-averaged and maximum values of turbulent Reynolds number are $Re_T \sim 4000$ and $\sim 10^5$, respectively. Here, $Re_T$ is based on the velocity scale, $u_T = (1/l_b)\int_{z_r=0}^{l_b} \sqrt{2K}\, dz_r$ where $K = 1/2 \langle u_i' u_i' \rangle$ is the turbulent kinetic energy, the length scale, $l_b$, and the

molecular viscosity, $\nu$. Variable time stepping with a fixed CFL number 1.2 is used leading to $\Delta\, t \simeq \mathcal{O}(1)$ sec. One tidal cycle takes approximately 1000 CPU hours.

## 3. Results

[9] The simulation starts with the phase of peak downslope velocity. There is transition to turbulence within approximately 3 hrs in the upper flank of the beam and in approximately 6 hrs at the bottom wall, followed by distinct turbulent mixing events that repeat periodically at different phases of the internal tide cycle as explained below.

[10] Figure 3 illustrates the phase variability of density and velocity by showing snapshots at four different times. Figure 3a at $t = 12.8$ hrs corresponds to a phase when the downslope flow is near its peak. The corresponding density deviation, $\rho^*$, is small and spans a short region, $0 < z < 20$ m. Inspection of Figures 3a–3d shows that $\rho^*$ lags $u$ by 90°; it is maximum when $u$ is minimum and vice-versa. At $t = 12.8$ hrs, the near-wall shear is large and, in the sheared zone of $0 < z < 20$ m, the corresponding density field in Figure 3e is indicative of both shear instability and fine scale turbulence. From $t = 12.8$ hrs until $t = 16$ hr when the velocity becomes approximately zero, the downward flow continues to bring water from above. Consequently, the region between 5 m and 30 m which, at $t = 12.8$ hrs was occupied by water with density shown by green in Figure 3e, is replaced by lighter, warmer water at $t = 16$ hrs, shown by red and yellow in Figure 3f. Furthermore, this body of relatively lighter, warmer water passes underneath the colder water above it that, being at the edge of the beam, has low velocity. The density profile that results at $t = 16$ hrs indicates a density inversion as shown in Figure 3b. The corresponding density
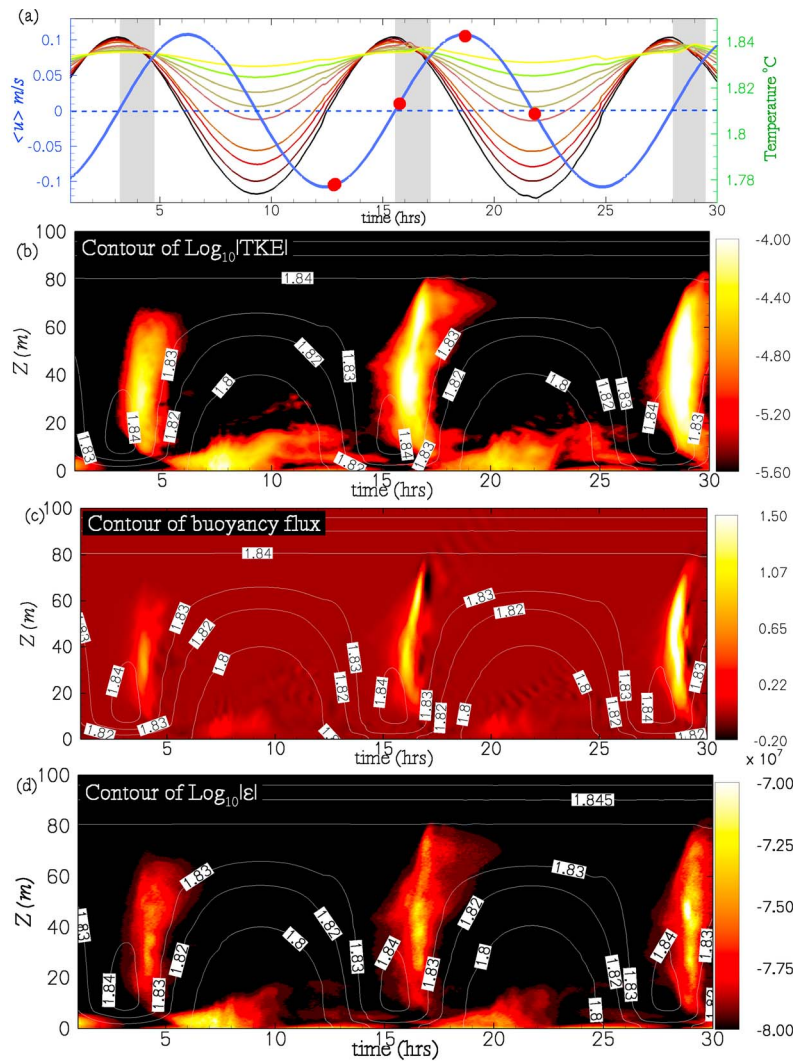
**Figure 4.** (a) Averaged along stream velocity (blue solid line) as function of time. Temperature is shown in same plot as function of time at different elevations from the sloping bottom, with black line corresponding to smallest elevation, $z* = 20$ m and yellow one showing for $z* = 60$ m. Flow reversal zone is shown by vertical grey colored bin. (b) Temporal evolution of spanwise averaged *TKE*, along a height. (c and d) Same as Figure 4b but for buoyancy flux and turbulent dissipation.

field in Figure 3f shows a mushroom shaped plume suggesting convective instability. The shear at this time is near zero. Note that the density inversion is even more prominent a little earlier at $t = 14.5$ hrs. Later in time, the large-scale overturns collapse and break into smaller structures. The shear starts increasing and at $t = 18.7$ hrs, the velocity profile in Figure 3c shows maximum upslope velocity and, correspondingly, the near wall flow is again susceptible to shear instability as shown in Figure 3g. The velocity in the next snapshot, Figure 3d, is almost zero and corresponds to $t = 21.4$ hrs when the flow reverses from up to down. Between $t = 18.7$ and 21.4 hrs, the flow decelerates but continues to move upslope and heavy, cold fluid associated with the central portion of the internal tide beam surges up beneath the lighter, low-velocity fluid above. The cumulative effect of this upsurge is to strengthen the stratification in the upper flank of the beam as shown by the region, $20 < z < 60$ m, in the density profile of Figure 3d. A the same time, the upsurge

overtakes low-velocity, lighter fluid near the wall leading to a density inversion with light fluid beneath dense fluid. Therefore, during flow reversal from up to down, a convective instability with the formation of a mushroom shaped structure occurs in the lower part of the flow as shown in Figure 3h. The height of the density overturn ($<15$ m) is significantly smaller than that observed earlier at $t = 16$ hr during flow reversal from down to up.

[11] Figures 4b–4d show the time evolution of vertical profiles of some turbulence statistics. $\langle \phi \rangle$, denotes an average of the quantity $\phi$ calculated by averaging over an $x_r - y_r$ plane parallel to the slope and we will show the dependence, $\langle \phi \rangle (z*, t)$, on height measured in meters above bottom (mab), $z*$, and time, $t$. Figure 4a shows streamwise velocity at 15 mab, to locate the phase of the internal tidal cycle. In Figure 4a, temperature is shown as a function of time at different elevations. It can be seen in Figure 4a that, during downward motion, e.g. $t = 10$ hrs to $t = 14$ hrs, the
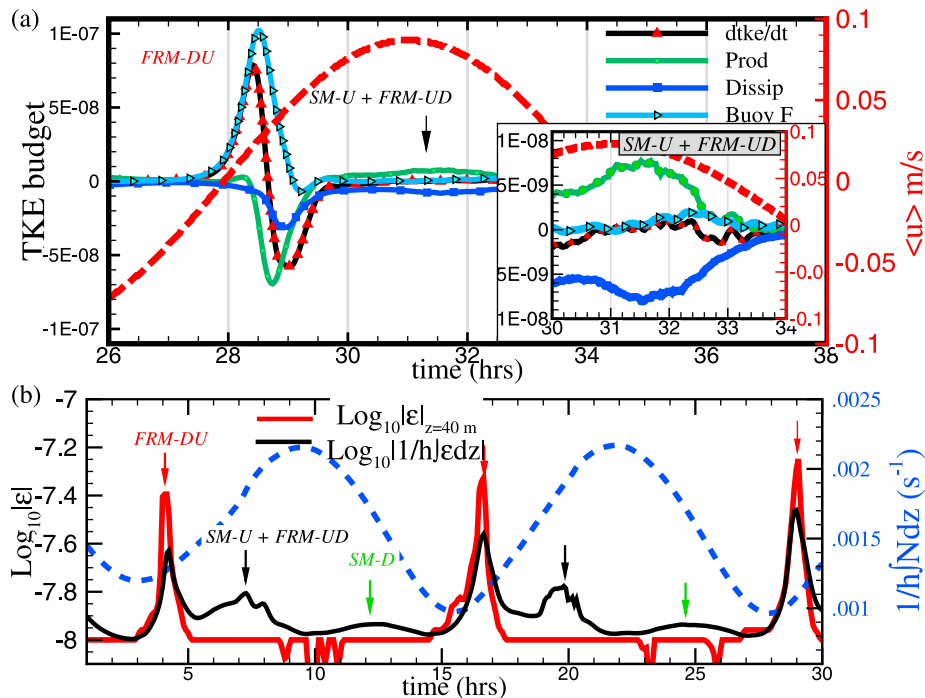
**Figure 5.** (a) Cycle evolution of depth-averaged values of the quantities in *TKE*-budget along with averaged streamwise velocity (dashed red line) at height of $z* = 25$ m. Here the averaging region extends from the bottom slope to $z* = 80$ m. (b) Temporal evolution of depth-averaged dissipation (black line) and buoyancy frequency $N$ (dashed blue line).

temperature at each $z*$ increases owing to warmer water coming down the slope from above. The rate of temperature increase is largest at $z* = 20$ mab which is near the center of the beam and progressively decreases for higher elevations. Therefore, the temperature (density) gradient in the region $20 < z* < 60$ progressively decreases in magnitude and, after $t \simeq 14$ hrs, the gradient reverses sign. The vertical span of the region with negative temperature gradient increases but such an unstable profile cannot be maintained for long and there is convective instability that develops into dissipative turbulence.

[12] Figure 4b shows turbulent kinetic energy (*TKE*) defined by $K = 1/2 \langle u_i' u_i' \rangle$, where $u_i' = u_i - \langle u_i \rangle$. Figures 4c and 4d show analogous plots for the buoyancy flux, $B = -(g/\rho_0) \langle \rho' w' \rangle$ and the turbulent dissipation rate, $\varepsilon$, calculated as the sum of resolved and subgrid dissipation rates. The combined effect of boundary velocity and density fields results in significant vertical variability of turbulent kinetic energy over a tidal cycle. Maximum *TKE* occurs away from the boundary and during flow reversal mixing from down to up (we will refer to such mixing events *FRM − DU*) at various time spans, $\Delta t \sim 3.1–4.8$, $15.5–17.2$ and $28–29.5$ hrs during the tidal cycle as shown by vertical grey colored bins in Figure 4a. Large positive buoyancy flux indicative of energy transfer from potential to kinetic energy occurs only during *FRM − DU* time intervals as shown in Figure 4c. Turbulent production, $P$, as well as dissipation, $\varepsilon$, are also large at that time. It is noteworthy that during these time intervals, the regions of large *TKE* and $\varepsilon$ are *detached* from the wall and extend up to a height of ~60–70 m.

[13] Shear production results in significant levels of turbulence when the upslope and down slope velocity are large; these mixing events are termed as *SM-U* and *SM-D*, respectively. During late deceleration (e.g. $8 < t < 10$), the turbulent dissipation peak also moves up and extends up a height of 20 m. Such an enhancement of dissipation away from the immediate vicinity of the bottom was not found by *Gayen et al.* [2010] and occurs here because of an additional physical mechanism, namely, convective instability during flow reversal mixing from up to down (*FRM − UD*) which was visualized earlier in Figure 3h.

[14] Figure 5a shows the temporal evolution of depth-averaged values of each term in the *TKE*-budget over a tidal period spanning $t = 26–38$ hrs. The depth-averaged buoyancy flux, $\langle B \rangle$, starts increasing at $t = 27.5$ at the onset of the *FRM − DU* event just prior to the zero-velocity phase, reaches its maximum value, and then plummets to zero at the end of the density overturn. Significant amount of negative production $\langle P \rangle$ occurs during the flow reversal event signaling the energy transfer from velocity fluctuations to the mean flow. The negative production, also seen in a companion DNS in a smaller domain, occurs because the turbulence is initiated by a positive buoyancy flux (not mean shear) and the mean shear changes sign after $u$ passes through zero. Soon after peak $\langle B \rangle$, the dissipation, $\langle \varepsilon \rangle$, increases. Production, $\langle P \rangle$, attains positive values immediately after the *FRM − DU* event. During the *SM − U* event as shown in the inset in Figure 5a, $\langle P \rangle$ and $\langle \varepsilon \rangle$ are the only dominant terms in the *TKE*-budget and both peak at the same time during the decelerating phase of upslope flow similar to the oscillatory boundary layer on a non-sloping bottom. At the end of the *SM − U* event and during the beginning of the *FRM − UD* event, the buoyancy flux, $\langle B \rangle$ regains positive values which are smaller relative to those during the *FRM − DU* event.

[15] Figure 5b quantifies the phase dependence of turbulent dissipation rate, $\varepsilon$, through a depth-averaged value. The

evolution of $\varepsilon$ at $z^* = 40$ m, a location at the upper flank of the internal tide beam, is also given to isolate the contribution of detached mixing events. $\varepsilon(z^* = 40, t)$ shows pronounced peaks, shown by the downward pointing arrows in red, that occur during $FRM - DU$. The elevated levels of dissipation occur over a time interval of approximately 1.5hrs. The depth-averaged $\varepsilon$ also shows peaks during $FRM - DU$. It is worth noting that at the onset of $FRM - DU$, the depth-averaged buoyancy frequency is minimum. Figure 5b shows additional time periods of elevated values of depth-averaged dissipation: one that occurs over a period of 1.5 hrs during the deceleration of upslope flow and is associated with $SM - U$ followed by $FRM - UD$, and another that occurs during shear mixing during down slope flow, $SM - D$.

[16] To place these simulation results in context, we compare with the bottom mooring observations by *Aucan et al.* [2006] taken during HOME. There is remarkable agreement between their observations and our simulations: (i) Density (potential temperature) records at different elevations converge at the $t \simeq 11$ point and then overturn as shown by *Aucan et al.* [2006, Figure 8a] similar to the shaded regions in Figure 4a, (ii) There is a large peak in turbulence and decrease in buoyancy frequency at the time corresponding to density overturns as shown by both *Aucan et al.* [2006, Figure 8b] and our Figure 4b, and (iii) Peak dissipation occurs when the across-flow velocity reverses from downslope to upslope, compare *Aucan et al.* [2006, Figure 8c] with blue curve in Figure 5a. *Gemmrich and van Haren* [2001] have observed thermal fronts associated with rapid fall of temperature above the continental slope in the Bay of Biscay. *Gemmrich and van Haren* [2001, Figure 4] show similarities with the sudden decrease of temperature after a plateau that occurs towards the end of FRM–DU events (shaded) in all the near-bottom temperature records shown in our Figure 4a.

## 4. Conclusion

[17] The interaction of an internal tide beam with a bottom slope has been examined using LES. The slope angle is taken to be 5°, and a beam with width of 60 m and a peak velocity of 0.125 m/s that propagates parallel to and across the slope is considered. The fine grid LES performed here allows space-time description of small-scale processes and enables quantification of turbulence and associated fluxes. Turbulent mixing events are found to repeat at specific phases in the internal tide cycle. Immediately after the zero velocity point when the flow reverses from down to upslope, there is a burst of turbulence with large dissipation that spans the beam and lasts for about 1.5 hours. This burst is initiated by a convective instability detached from the bottom and is accompanied by a large positive buoyancy flux. There are also phases corresponding to peak tidal velocity when there is turbulence closer to the bottom that is driven by bottom shear. The present study considered a internal wave beam with a velocity profile corresponding to an internal tide generation site. Nevertheless, it is expected that an internal wave beam generated nearby that grazes the bottom will also lead to similar bottom mixing processes. The phasing and other characteristics of the beam-scale convectively-driven mixing in the present simulations show remarkable similarity to observations by *Aucan et al.* [2006] at a bottom mooring in the path of a internal wave beam generated at a nearby critical slope. The bottom mixing process, mediated by an internal tide beam during generation or propagation from a nearby generation site, is likely to be important in other situations with rough topography and the parametric dependence of this process on environmental parameters is worth future study.

## References

Aucan, J., M. A. Merrifield, D. S. Luther, and P. Flament (2006), Tidal mixing events on the deep flanks of Kaena Ridge, Hawaii, *J. Phys. Oceanogr.*, *36*, 1202–1219.
Gayen, B., and S. Sarkar (2010), Turbulence during the generation of internal tide on a critical slope, *Phys. Rev. Lett.*, *104*, 218502.
Gayen, B., and S. Sarkar (2011), Direct and large eddy simulations of internal tide generation at a near critical slope, *J. Fluid Mech.*, doi:10.1017/jfm.2011.170, in press.
Gayen, B., S. Sarkar, and J. R. Taylor (2010), Large eddy simulation of a stratified boundary layer under an oscillatory current, *J. Fluid Mech.*, *643*, 233–266.
Gemmrich, J. R., and H. van Haren (2001), Thermal fronts generated by internal waves propagating obliquely along the continental slope, *J. Phys. Oceanogr.*, *31*, 649–655.
Klymak, J. M., J. N. Moum, J. D. Nash, E. Kunze, J. B. Girton, G. S. Carter, C. M. Lee, T. B. Sanford, and M. C. Gregg (2006), An estimate of tidal energy lost to turbulence at the Hawaiian Ridge, *J. Phys. Oceanogr.*, *36*, 1148–1164.
Kunze, E., and J. M. Toole (1997), Tidally driven vorticity, diurnal shear and turbulence atop Fieberling Seamount, *J. Phys. Oceanogr.*, *27*, 2663–2693.
Ledwell, J. R., E. T. Montgomery, K. L. Polzin, L. C. St. Laurent, R. W. Schmitt, and J. M. Toole (2000), Evidence of enhanced mixing over rough topography in the abyssal ocean, *Nature*, *403*, 179–182.
Levine, M. D., and T. J. Boyd (2006), Tidally forced internal waves and overturns observed on a slope: Results from HOME, *J. Phys. Oceanogr.*, *36*, 1184–1201.
Lim, K., G. N. Ivey, and N. L. Jones (2010), Experiments on the generation of internal waves over continental shelf topography, *J. Fluid Mech.*, *663*, 385–400.
Lueck, R. G., and T. D. Mudge (1997), Topographically induced mixing around a shallow seamount, *Science*, *276*, 1831–1833.
Moum, J. N., D. R. Caldwell, J. D. Nash, and G. D. Gunderson (2002), Observations of boundary mixing over the continental slope, *J. Phys. Oceanogr.*, *32*, 2113–2130.
Nash, J. D., M. H. Alford, E. Kunze, K. Martini, and S. Kelly (2007), Hotspots of deep ocean mixing on the Oregon continental slope, *Geophys. Res. Lett.*, *34*, L01605, doi:10.1029/2006GL028170.
Polzin, K. L., J. M. Toole, J. R. Ledwell, and R. W. Schmitt (1997), Spatial variability of turbulent mixing in the abyssal ocean, *Science*, *276*, 93–96.
Rudnick, D. L., et al. (2003), From tides to mixing along the Hawaiian Ridge, *Science*, *301*, 355–357.
St. Laurent, L. C., J. M. Toole, and R. W. Schmitt (2001), Buoyancy forcing by turbulence above rough topography in the abyssal Brazil Basin, *J. Phys. Oceanogr.*, *31*, 3476–3495.
Thorpe, S. A., P. Hall, and M. White (1990), The variability of mixing at the continental slope, *Philos. Trans. R. Soc. London, Ser. A, 331*, 183–194.

B. Gayen and S. Sarkar, Mechanical and Aerospace Engineering Department, University of California, San Diego, La Jolla, CA 92093, USA. (sarkar@ucsd.edu)